




LRD spectral analysis of multifractional functional time series on manifolds

Diana P. Ovalle–Muñoz¹ · M. Dolores Ruiz–Medina¹ 

Received: 26 December 2022 / Accepted: 2 December 2023
© The Author(s) 2024, corrected publication 2024

Abstract

This paper addresses the estimation of the second-order structure of a manifold cross-time random field (RF) displaying spatially varying Long Range Dependence (LRD), adopting the functional time series framework introduced in Ruiz-Medina (Fract Calc Appl Anal 25:1426–1458, 2022). Conditions for the asymptotic unbiasedness of the integrated periodogram operator in the Hilbert–Schmidt operator norm are derived beyond structural assumptions. Weak-consistent estimation of the long-memory operator is achieved under a semiparametric functional spectral framework in the Gaussian context. The case where the projected manifold process can display Short Range Dependence (SRD) and LRD at different manifold scales is also analyzed. The performance of both estimation procedures is illustrated in the simulation study, in the context of multifractionally integrated spherical functional autoregressive–moving average (SPHARMA(p,q)) processes.

Keywords Connected and compact two-point homogeneous spaces · Ibragimov contrast function · LRD multifractionally integrated functional time series · Manifold cross-time RFs · Multifractional spherical stochastic partial differential equations

Mathematics Subject Classification 60G10 · 60G12 · 60G18 · 60G20 · 60G22 (primary) · 60G60

1 Introduction

The literature on weakly dependent functional time series has been widely developed in the last few decades, allowing the statistical analysis, and inference on stochastic processes under a Markovian framework (see, e.g., Bosq (2000), Horváth and Kokoszka (2012)). Nowadays, spectral analysis of functional time series models constitutes an

✉ M. Dolores Ruiz–Medina
mruiz@ugr.es

¹ Faculty of Sciences, University of Granada, Avd, Fuente Nueva s/n, 18071 Granada, Spain

open research area. Under suitable functional cumulant mixing conditions, and the summability in time of the trace norm of the elements of the covariance operator family, in Panaretos and Tavakoli (2013a), a weighted periodogram operator estimator of the spectral density operator is derived. Its asymptotic analysis is addressed. Particularly, the asymptotic normality of the functional discrete Fourier transform (fDFT) of the curve data is proved (see also Tavakoli (2014)). In Panaretos and Tavakoli (2013b), a harmonic principal component analysis of functional time series, based on Karhunen–Loève–like decomposition in the temporal functional spectral domain is proposed, the so-called Cramér–Karhunen–Loève representation (see also Rubín and Panaretos (2020a), Rubín and Panaretos (2020b)). Some recent applications in the context of functional regression are obtained in Pham and Panaretos (2018). Hypothesis testing for detecting modeling differences in functional time series dynamics is achieved in Tavakoli and Panaretos (2016) in the functional spectral domain.

Recently, an attempt to extend spectral analysis of functional time series to the context of LRD functional sequences has been presented in Ruiz–Medina (2022), covering, in particular, some examples of the LRD functional time series family analyzed in Li et al. (2019) in the temporal domain. The application of harmonic analysis in this more general context entails important advantages as given in Ruiz–Medina (2022). Particularly, under stationary in time, the temporal dependence range can be approximated from the behavior in a neighborhood of zero frequency of the spectral density operator family at different spatial resolution levels. Moreover, a more flexible modeling framework can be introduced in this setting. Particularly, the projected process can display LRD and SRD depending on the spatial scale, according to the support of the spectral measure of the LRD operator characterizing the distribution of its eigenvalues. In Li et al. (2019), Functional Principal Component Analysis (FPCA), based on the long-run covariance function, is applied in the consistent estimation of the dimension and the orthonormal functions spanning the dominant subspace, where the projected curve process displays the largest dependence range. Fractionally integrated functional autoregressive moving averages processes constitute an interesting example (see Li et al. (2019)). The multifractionally integrated version of this process family can be analyzed under the modeling framework introduced in Ruiz–Medina (2022).

Connected and compact two-point homogeneous spaces constitute an example of manifold, with isometrically equivalent properties to the sphere, locally resembles an Euclidean space. Here, we will denote it as \mathbb{M}_d , with d being its topological dimension. The isotropy or invariance of a kernel with respect to the group of isometries of \mathbb{M}_d allows its diagonal representation in terms of a fixed orthonormal basis given by the eigenfunctions of the Laplace–Beltrami operator on $L^2(\mathbb{M}_d, d\nu)$. Thus, the separable Hilbert space $H = L^2(\mathbb{M}_d, d\nu)$ of square integrable functions on \mathbb{M}_d is considered in our functional time series analysis. Here, $d\nu$ is the normalized Riemannian measure on \mathbb{M}_d . Particularly, this Hilbert space framework has been adopted by several authors in the current literature for the special case of the sphere. That is the case of Caponera and Marinucci (2021), where estimation and asymptotic analysis of spherical functional time series is achieved, introducing new model families (see Caponera (2021)). Also, in the LRD framework, sphere cross-time random fields are analyzed in Marinucci et al. (2020), investigating the asymptotic behavior, under temporal increasing domain, of the empirical measure of a excursion area at any threshold.

Time-dependent RF solution to a fractional pseudodifferential equation on the sphere is introduced in D' Ovidio et al. (2016) (see also Anh et al. (2018)). The eigenfunctions of the Laplace Beltrami operator on $L^2(\mathbb{M}_d, d\nu)$, and the corresponding zonal functions play a crucial role in the analysis of manifold cross-time random fields (see, e.g., Ma and Malyarenko (2020)). For example, Sobolev regularity and Hölder continuity of Gaussian RFs on a connected and compact two-point homogeneous space are studied in Cleanthous et al. (2020) and Cleanthous et al. (2021), by exploiting asymptotic properties of the pure point spectra of invariant kernels, and projection of functions into the eigenfunctions of the Laplace Beltrami operator. Some motivating real data applications can be found in the field of Cosmic Microwave Background (CMB) radiation (see, e.g., Marinucci and Peccati (2011) and references therein). It is well-known the interest of these RFs in climatic change analysis (see, e.g., Alegría et al. (2021)).

The spectral domain allows to characterize LRD in functional time series in terms of the unboundedness at zero frequency of the corresponding element of the family of spectral density operators. Specifically, the divergence of the eigenvalues of the elements of the spectral density operator family at a neighborhood of zero frequency leads to different levels of singularity at this frequency depending on the spatial scale (see, e.g., Ruiz-Medina (2022)). The case of SRD and LRD at different spatial scales can also be analyzed, in the case of non-trivial null space of the LRD operator. Thus, the projected process displays SRD in this subspace, and LRD in the eigenspaces associated with the elements of the support of the spectral measure of the LRD operator.

From a theoretical point of view, this paper contributes providing a sufficient condition for the asymptotic unbiasedness of the integrated periodogram operator, in the Hilbert–Schmidt operator norm, for the class of zero-mean, stationary and isotropic, mean-square continuous Gaussian, or elliptically contoured, spatiotemporal RFs on \mathbb{M}_d . This result provides a suitable setting for applying the LRD spectral functional time series framework introduced in Ruiz-Medina (2022), where the weak-consistent estimation of the second-order structure in the functional spectral domain is achieved under a Gaussian scenario. Our scenario is a bit different, since the Hilbert–Schmidt operator scenario has been considered. Note that this scenario has usually been adopted in the current literature on functional time series (see Bosq (2000), Caponera and Marinucci (2021)). The case where SRD and LRD are displayed at different manifold scales is also addressed, combining semiparametric estimation of the spectral density operator based on minimum contrast at manifold scales where LRD is displayed, and a nonparametric estimation based on the weighted periodogram operator in the remaining manifold scales where SRD is observed. The preliminary result derived in the Supplementary Material on spatiotemporal Karhunen–Loève expansion of the restriction to a bounded closed temporal interval of a zero-mean, stationary in time and isotropic in space, mean-square continuous Gaussian spatiotemporal RF on \mathbb{M}_d has been applied.

From a practical point of view, the simulation study undertaken in Sect. 5 illustrates the performance beyond the Gaussian scenario of the two proposed estimation approaches in the functional spectral domain, in the context of multifractionally integrated SPHARMA(p,q) processes. Two cases are analyzed respectively corresponding to a decreasing and increasing positive bounded eigenvalue sequence of the LRD oper-

ator. Particularly, we study the scenario where the projected process displays SRD and LRD at different spherical scales. This last case is illustrated when the eigenvalues of the LRD operator vanish at high discrete Legendre frequencies. Details on the implementation of both estimation methodologies, and some conclusions on the results obtained beyond the Gaussian scenario are also included in Sects. 5–6 (see also the Supplementary Material).

The outline of the paper is the following. Section 2 introduces notation, technical tools and preliminary elements. Asymptotic unbiasedness of the integrated periodogram operator, and weak consistent minimum contrast estimation are studied in Sect. 3. An extended formulation of this estimation methodology to the case where temporal LRD and SRD are displayed at different manifold scales is proposed in Sect. 4. A simulation study is undertaken in Sect. 5 to illustrate the performance of the proposed estimation methodologies. A summary of conclusions about the simulation study is given in Sect. 6. The Supplementary Material complements the theoretical material about the paper, and provides the results of the simulation study in the remaining scenarios analyzed that are not displayed in the paper.

2 Preliminaries

The family of manifold cross-time RFs analyzed in this paper is introduced in this section. The connected and compact two-point homogeneous spaces are briefly described, providing some preliminary algebraic notions, with reference to the invariant probabilistic measure, and the Laplace Beltrami operator.

Let $X = \{X(\mathbf{x}, t), \mathbf{x} \in \mathbb{M}_d, t \in \mathbb{T}\}$ be a wide sense stationary in time and isotropic in space zero-mean, and mean-square continuous Gaussian, or elliptically contoured, RF on the basic probability space (Ω, \mathcal{A}, P) . Here, \mathbb{T} denotes the temporal domain, which usually is \mathbb{Z} or \mathbb{R} (see also the Supplementary Material for the case of a bounded temporal interval $[0, T]$). Assume also that the map $\tilde{X}_t : (\Omega, \mathcal{A}) \rightarrow (L^2(\mathbb{M}_d, d\nu), \mathcal{B}(L^2(\mathbb{M}_d, d\nu)))$ is measurable, with $\tilde{X}_t(\mathbf{x}) := X(\mathbf{x}, t)$ for every $t \in \mathbb{T}$ and $\mathbf{x} \in \mathbb{M}_d$. Here, $\mathcal{B}(L^2(\mathbb{M}_d, d\nu))$ denotes the σ -algebra generated by all cylindrical subsets of $L^2(\mathbb{M}_d, d\nu)$.

Let $d_{\mathbb{M}_d}$ be the geodesic distance induced by the isometry with the unit sphere, preserving the spherical distance $\rho(\mathbf{x}, \mathbf{y}) = \cos^{-1}(\langle \mathbf{x}, \mathbf{y} \rangle)$, $\mathbf{x}, \mathbf{y} \in \mathbb{S}_d$, and let $\omega_d = \int_{\mathbb{M}_d} d\nu(\mathbf{x})$. In the following, $R_n^{(\alpha, \beta)}(\cos(d_{\mathbb{M}_d}(\mathbf{x}, \mathbf{y}))) = \frac{P_n^{(\alpha, \beta)}(\cos(d_{\mathbb{M}_d}(\mathbf{x}, \mathbf{y})))}{P_n^{(\alpha, \beta)}(1)}$, with $P_n^{(\alpha, \beta)}$ being the Jacobi polynomial of degree n with a pair of parameters (α, β) (see, e.g., Andrews et al. (1999)). For each $n \in \mathbb{N}_0$, $\{S_{n,1}^d, \dots, S_{n,\delta(n,d)}^d\}$ is the orthonormal basis of eigenfunctions of the eigenspace H_n of Laplace–Beltrami operator Δ_d on $L^2(\mathbb{M}_d, d\nu)$, associated with the eigenvalue $\lambda_n = -n\varepsilon(n\varepsilon + \alpha + \beta + 1)$. The dimension $\delta(n, d)$ of H_n is given by

$$\delta(n, d) = \frac{(2n + \alpha + \beta + 1)\Gamma(\beta + 1)\Gamma(n + \alpha + \beta + 1)\Gamma(n + \alpha + 1)}{\Gamma(\alpha + 1)\Gamma(\alpha + \beta + 2)\Gamma(n + 1)\Gamma(n + \beta + 1)}.$$

Note that $\alpha = (p + q - 1)/2$, $\beta = (q - 1)/2$, and $\varepsilon = 2$ if $\mathbb{M}_d = \mathbb{P}^d(\mathbb{R})$, the projective space over the field \mathbb{R} , and $\varepsilon = 1$, otherwise. Parameters q and p are the dimensions of some root spaces connected with the Lie algebras of the groups G and K , with $\mathbb{M}_d \simeq G/K$, being G the connected component of the group of isometries of \mathbb{M}_d , and K the stationary subgroup of a fixed point \mathbf{o} in \mathbb{M}_d (see, e.g., Table 1 in Ma and Malyarenko (2020)).

The next lemma is applied along the paper.

Lemma 1 (See (Giné (1975), Theorem 3.2.) and (Andrews et al. (1999), p 455)) For every $n \in \mathbb{N}_0$, the following addition formula holds:

$$\sum_{j=1}^{\delta(n,d)} S_{n,j}^d(\mathbf{x}) S_{n,j}^d(\mathbf{y}) = \frac{\delta(n,d)}{\omega_d} R_n^{\alpha,\beta}(\cos(d_{\mathbb{M}_d}(\mathbf{x}, \mathbf{y}))), \quad \mathbf{x}, \mathbf{y} \in \mathbb{M}_d. \quad (2.1)$$

Let $C(d_{\mathbb{M}_d}(\mathbf{x}, \mathbf{y}), t - s) = E[X(\mathbf{x}, t)X(\mathbf{y}, s)]$, for $\mathbf{x}, \mathbf{y} \in \mathbb{M}_d$, and $t, s \in \mathbb{T}$, be the covariance function of X . Assume that $C(d_{\mathbb{M}_d}(\mathbf{x}, \mathbf{y}), t) = C(d_{\mathbb{M}_d}(\mathbf{x}, \mathbf{y}), -t)$. The following diagonal series expansion holds under the conditions of Theorem 4 in Ma and Malyarenko (2020):

$$\begin{aligned} C(d_{\mathbb{M}_d}(\mathbf{x}, \mathbf{y}), t - s) &= \sum_{n \in \mathbb{N}_0} B_n(t - s) \sum_{j=1}^{\delta(n,d)} S_{n,j}^d(\mathbf{x}) S_{n,j}^d(\mathbf{y}) \\ &= \sum_{n \in \mathbb{N}_0} \frac{\delta(n,d)}{\omega_d} B_n(t - s) R_n^{\alpha,\beta}(\cos(d_{\mathbb{M}_d}(\mathbf{x}, \mathbf{y}))), \quad \mathbf{x}, \mathbf{y} \in \mathbb{M}_d, t, s \in \mathbb{T}. \end{aligned} \quad (2.2)$$

3 Operator-based minimum contrast parameter estimation of LRD

This section adopts the semiparametric spectral LRD functional time series framework introduced in Ruiz-Medina (2022) (see **Condition C1** below), for inference on an LRD manifold cross-time RF, constructed from a zero-mean, stationary in time, and isotropic in space, mean-square continuous Gaussian, or elliptically contoured spatiotemporal RF $X = \{X(\mathbf{x}, t), \mathbf{x} \in \mathbb{M}_d, t \in \mathbb{T} = \mathbb{Z}\}$ (see, e.g., Marinucci et al. (2020) for sphere cross-time RFs).

Note that under the conditions assumed in Sect. 2, $X = \{X(\mathbf{x}, t), \mathbf{x} \in \mathbb{M}_d, t \in \mathbb{T} = \mathbb{Z}\}$ defines a functional time series $\{\tilde{X}_t(\cdot), t \in \mathbb{Z}\}$. In Sect. 3.1 below, we will work under this scenario to implement minimum contrast parameter estimation under **Condition C1** (providing the semiparametric functional spectral framework introduced in Ruiz-Medina (2022)).

Condition C0 below establishes a sufficient condition for the asymptotic unbiasedness of the integrated periodogram operator of X in the Hilbert-Schmidt operator norm beyond structural assumptions (see Theorem 1). The weak-consistency of the minimum contrast estimator of the LRD operator is then obtained in

Theorem 2, under new **Condition C0** and **Condition C1**, adopting the $L^2(\mathbb{M}_d, d\nu)$ -valued time series framework.

The following condition will be assumed in the subsequent development.

Condition C0. The elements of the temporal coefficient sequence $\{B_n(\tau), n \in \mathbb{N}_0\}$ in Eq. (2.2) are such that

$$\sum_{n \in \mathbb{N}_0} \delta(n, d) \sum_{\tau \in \mathbb{Z}} B_n^2(\tau) < \infty. \tag{3.1}$$

Under condition (3.1) (see Eq. (3.3) below), one can define almost surely (a.s.) in $\omega \in [-\pi, \pi]$, i.e., $\omega \in [-\pi, \pi] \setminus \mathcal{D}_0$, $\int_{\mathcal{D}_0} d\omega = 0$, the spectral density operator \mathcal{F}_ω in the space $\mathcal{S}(L^2(\mathbb{M}_d, d\nu; \mathbb{C}))$ of Hilbert–Schmidt operators on $L^2(\mathbb{M}_d, d\nu; \mathbb{C})$ as follows:

$$\mathcal{F}_\omega \Big|_{\mathcal{S}(L^2(\mathbb{M}_d, d\nu; \mathbb{C}))} = \frac{1}{2\pi} \sum_{\tau \in \mathbb{Z}} \exp(-i\omega\tau) \mathcal{R}_\tau, \tag{3.2}$$

where $\mathcal{R}_\tau = E[\tilde{X}_s \otimes \tilde{X}_{s+\tau}] = E[\tilde{X}_{s+\tau} \otimes \tilde{X}_s]$, for $\tau, s \in \mathbb{Z}$.

Note that Parseval identity leads to

$$\begin{aligned} \int_{-\pi}^{\pi} \|\mathcal{F}_\omega\|_{\mathcal{S}(L^2(\mathbb{M}_d, d\nu; \mathbb{C}))}^2 d\omega &= \sum_{n \in \mathbb{N}_0} \delta(n, d) \int_{-\pi}^{\pi} |f_n(\omega)|^2 d\omega \\ &= \sum_{n \in \mathbb{N}_0} \delta(n, d) \sum_{\tau \in \mathbb{Z}} B_n^2(\tau) = \sum_{\tau \in \mathbb{Z}} \|\mathcal{R}_\tau\|_{\mathcal{S}(L^2(\mathbb{M}_d, d\nu; \mathbb{R}))}^2 < \infty. \end{aligned} \tag{3.3}$$

From Eqs. (2.2) and (3.3), \mathcal{F}_ω has kernel $f_\omega(\mathbf{x}, \mathbf{y})$, $\mathbf{x}, \mathbf{y} \in \mathbb{M}_d$, admitting for $\omega \in [-\pi, \pi] \setminus \mathcal{D}_0$, the following diagonal series expansion in the space $\mathcal{S}(L^2(\mathbb{M}_d, d\nu; \mathbb{C})) \equiv L^2(\mathbb{M}_d \times \mathbb{M}_d, d\nu \otimes d\nu; \mathbb{C})$: For $\mathbf{x}, \mathbf{y} \in \mathbb{M}_d$,

$$\begin{aligned} f_\omega(\mathbf{x}, \mathbf{y}) \Big|_{L^2(\mathbb{M}_d \times \mathbb{M}_d)} &= \frac{1}{2\pi} \sum_{n \in \mathbb{N}_0} f_n(\omega) \sum_{j=1}^{\delta(n, d)} S_{n, j}^d(\mathbf{x}) S_{n, j}^d(\mathbf{y}) \\ &= \frac{1}{2\pi} \sum_{n \in \mathbb{N}_0} \left[\sum_{\tau \in \mathbb{Z}} \exp(-i\omega\tau) B_n(\tau) \right] \frac{\delta(n, d)}{\omega_d} R_n^{(\alpha, \beta)}(\cos(d_{\mathbb{M}_d}(\mathbf{x}, \mathbf{y}))). \end{aligned} \tag{3.4}$$

The convergence to zero in the Hilbert–Schmidt operator norm of the integrated bias of the periodogram operator also holds under (3.1).

Theorem 1 Under condition (3.1),

$$\left\| \int_{-\pi}^{\pi} [\mathcal{F}_\omega - \mathcal{F}_\omega^{(T)}] d\omega \right\|_{\mathcal{S}(L^2(\mathbb{M}_d, d\nu; \mathbb{C}))} \rightarrow 0, \quad T \rightarrow \infty,$$

where $\mathcal{F}_\omega^{(T)}$ denotes the mean of the periodogram operator

$$p_\omega^{(T)} = \tilde{X}_\omega^{(T)} \otimes \overline{\tilde{X}_\omega^{(T)}}, \quad \omega \in [-\pi, \pi],$$

with $\tilde{X}_\omega^{(T)}(\cdot) \stackrel{L^2(\mathbb{M}_d, d\nu; \mathbb{C})}{=} \frac{1}{\sqrt{2\pi T}} \sum_{t=1}^T \tilde{X}_t(\cdot) \exp(-i\omega t)$, $\omega \in [-\pi, \pi]$, being the functional Discrete Fourier Transform (fDFT), based on a functional sample \tilde{X}_t , $t = 1, \dots, T$, of spatiotemporal RF X . Here, as before, for each $t = 1, \dots, T$, $\tilde{X}_t(\mathbf{x}) := X(\mathbf{x}, t)$, for every $\mathbf{x} \in \mathbb{M}_d$.

Proof The proof follows from Eq. (3.3) implying Lemma 1 in Ruiz-Medina (2022) holds in our context. Hence, Eqs. (4.6)–(4.8) in the proof of Theorem 1 in Ruiz-Medina (2022), and the remaining steps of the proof of this theorem can be obtained in a similar way. □

3.1 Minimum contrast parameter estimation

For the implementation of the minimum contrast parameter estimation of the spatial-varying LRD parameter of X , in the $L^2(\mathbb{M}_d, d\nu)$ -valued time series framework introduced in Ruiz-Medina (2022), the following condition is assumed:

Condition C1. The elements of the function sequence of Fourier transforms $\{f_n(\cdot), n \in \mathbb{N}_0\}$ in (3.4) admit the following semiparametric modeling: For every $\omega \in [-\pi, \pi] \setminus \{0\}$,

$$f_{n,\theta}(\omega) = B_n^\eta(0)M_n(\omega) \left[4(\sin(\omega/2))^2\right]^{-\alpha(n,\theta)/2}, \quad \theta \in \Theta, \quad n \in \mathbb{N}_0, \quad (3.5)$$

where $l_\alpha(\theta) \leq \alpha(n, \theta) \leq L_\alpha(\theta)$, for any $n \geq 0$, and $\theta \in \Theta$, for certain $l_\alpha(\theta), L_\alpha(\theta) \in (0, 1/2)$. The elements of the function sequence $\{M_n, n \in \mathbb{N}_0\}$ are strictly positive continuous functions on $[-\pi, \pi]$, slowly varying at zero frequency in the Zygmund’s sense (see, e.g., Definition 6.6 in Beran (2017)). For every $\omega \in [-\pi, \pi]$, $\{M_n(\omega), n \in \mathbb{N}_0\}$ are the eigenvalues of operator $\mathcal{M}_\omega \in \mathcal{S}(L^2(\mathbb{M}_d, d\nu; \mathbb{C}))$, and $\|\mathcal{M}_\omega\|_{\mathcal{S}(L^2(\mathbb{M}_d, d\nu; \mathbb{C}))} \in L^2([-\pi, \pi])$. The operator family $\{\mathcal{M}_\omega, \omega \in [-\pi, \pi]\}$ defines the SRD spectral family. The associated kernel family satisfies

$$\begin{aligned} \mathcal{K}_{\mathcal{M}_\omega}(\mathbf{x}, \mathbf{y}) &= \sum_{n \in \mathbb{N}_0} M_n(\omega) \sum_{j=1}^{\delta(n,d)} S_{n,j}^d(\mathbf{x}) S_{n,j}^d(\mathbf{y}) \\ &= \sum_{n \in \mathbb{N}_0} M_n(\omega) \frac{\delta(n,d)}{\omega_d} R_n^{(\alpha,\beta)}(\cos(d_{\mathbb{M}_d}(\mathbf{x}, \mathbf{y}))), \quad \mathbf{x}, \mathbf{y} \in \mathbb{M}_d. \end{aligned}$$

The parameter space Θ is assumed to be compact with non-null interior. For each $\theta \in \Theta$, $\{\alpha(n, \theta), n \in \mathbb{N}_0\}$ is the system of eigenvalues of the parameterized long-memory operator \mathcal{A}_θ with kernel $\mathcal{K}_{\mathcal{A}_\theta}$ admitting the following diagonal series

expansion:

$$\begin{aligned} \mathcal{K}_{\mathcal{A}_\theta}(\mathbf{x}, \mathbf{y}) &= \sum_{n \in \mathbb{N}_0} \alpha(n, \theta) \sum_{j=1}^{\delta(n,d)} S_{n,j}^d(\mathbf{x}) S_{n,j}^d(\mathbf{y}) \\ &= \sum_{n \in \mathbb{N}_0} \alpha(n, \theta) \frac{\delta(n, d)}{\omega_d} R_n^{(\alpha, \beta)}(\cos(d_{\mathbb{M}_d}(\mathbf{x}, \mathbf{y}))), \quad \mathbf{x}, \mathbf{y} \in \mathbb{M}_d. \end{aligned}$$

Hence, for every $\theta \in \Theta$, \mathcal{A}_θ has isotropic kernel and defines a strictly positive self-adjoint operator on $L^2(\mathbb{M}_d, d\nu)$, with norm in the space $\mathcal{L}(L^2(\mathbb{M}_d, d\nu))$ of bounded linear operators less than $1/2$. Note that, since $\sin(\omega) \sim \omega$, $\omega \rightarrow 0$,

$$|1 - \exp(-i\omega)|^{-\mathcal{A}_\theta} = [4 \sin^2(\omega/2)]^{-\mathcal{A}_\theta/2} \sim |\omega|^{-\mathcal{A}_\theta}, \quad \omega \rightarrow 0, \tag{3.6}$$

where the frequency varying operator $|1 - \exp(-i\omega)|^{-\mathcal{A}_\theta/2}$ is interpreted as in Characiejus and Ráckauskas (2014), Rackauskas and Suquet (2011). In particular, Eq. (3.1) in **Assumption II** in Ruiz-Medina (2022), characterizing LRD of functional time series in the spectral domain, holds.

Remark 1 **Condition C1** restricts the eigenvalues of \mathcal{A}_θ to the interval $(0, 1/2)$, leading to a shorter range of spectral singularity at zero frequency at any spatial scale, allowing (3.3) holds. In particular,

$$\begin{aligned} \int_{-\pi}^{\pi} \|\mathcal{F}_\omega\|_{\mathcal{S}(L^2(\mathbb{M}_d, d\nu; \mathbb{C}))}^2 d\omega &= \sum_{n \in \mathbb{N}_0} \delta(n, d) \int_{-\pi}^{\pi} |f_n(\omega)|^2 d\omega \\ &\leq \left\{ \left[\int_{-\pi}^{-1} + \int_1^{\pi} \right] |\omega|^{-2l(\theta)} + \int_{-1}^1 |\omega|^{-2L(\theta)} \right\} \|\mathcal{M}_\omega\|_{\mathcal{S}(L^2(\mathbb{M}_d, d\nu; \mathbb{C}))}^2 d\omega < \infty. \end{aligned} \tag{3.7}$$

The sequence $\{B_n^\eta(0) \geq 0, n \in \mathbb{N}_0\}$ in Eq. (3.5) defines the eigenvalues of the trace integral autocovariance operator $\mathcal{R}_0^\eta = E[\eta_t \otimes \eta_t] = E[\eta_0 \otimes \eta_0]$, $t \in \mathbb{Z}$, of the zero-mean innovation process $\{\eta_t, t \in \mathbb{Z}\}$, with kernel r_η satisfying

$$r_\eta(\mathbf{x}, \mathbf{y}) = \sum_{n \in \mathbb{N}_0} B_n^\eta(0) \sum_{j=1}^{\delta(n,d)} S_{n,j}^d(\mathbf{x}) S_{n,j}^d(\mathbf{y}), \quad \forall \mathbf{x}, \mathbf{y} \in \mathbb{M}_d,$$

where $\frac{B_n(0)}{B_n^\eta(0)} = \int_{-\pi}^{\pi} M_n(\omega) [4(\sin(\omega/2))^2]^{-\alpha(n,\theta)/2} d\omega$, for each $n \in \mathbb{N}_0$.

Assume that the true parameter value θ_0 lies in the non-empty interior of compact set Θ , and $\alpha(\cdot, \theta_1) \neq \alpha(\cdot, \theta_2)$, for $\theta_1 \neq \theta_2$, and $\theta_1, \theta_2 \in \Theta$, ensuring identifiability. Let $\{\hat{\alpha}_T(n, \theta) = \alpha(n, \hat{\theta}_T), n \in \mathbb{N}_0\}$ be the parametric estimators of the eigenvalues of \mathcal{A}_θ by minimum contrast. The computation of the minimum contrast parametric estimator $\hat{\theta}_T$ requires the introduction of some operator families in the spectral domain as now briefly describe.

Operator integrals are understood here as improper operator Stieltjes integrals which strongly converge (see, e.g., Sect. 8.2.1 in Ramm (2005)). Specifically, in the definition of our loss function, integration in the temporal spectral domain with respect to weighting operator \mathcal{W}_ω is achieved. For each $\omega \in [-\pi, \pi]$, the invariant kernel $\mathcal{K}_{\mathcal{W}_\omega}$ of \mathcal{W}_ω on $\mathbb{M}_d \times \mathbb{M}_d$ admits the following series expansion:

$$\begin{aligned} \mathcal{K}_{\mathcal{W}_\omega}(\mathbf{x}, \mathbf{y}) &= \sum_{n \in \mathbb{N}_0} W(\omega, n, \gamma) \sum_{j=1}^{\delta(n,d)} S_{n,j}^d(\mathbf{x}) S_{n,j}^d(\mathbf{y}) \\ &= \sum_{n \in \mathbb{N}_0} \tilde{W}(n) |\omega|^\gamma \sum_{j=1}^{\delta(n,d)} S_{n,j}^d(\mathbf{x}) S_{n,j}^d(\mathbf{y}), \quad \gamma > 0, \mathbf{x}, \mathbf{y} \in \mathbb{M}_d, \end{aligned} \tag{3.8}$$

where the eigenvalues $\{W(\omega, n, \gamma), n \in \mathbb{N}_0\}$ factorize as $W(\omega, n, \gamma) = \tilde{W}(n) |\omega|^\gamma$, for every $n \in \mathbb{N}_0$, with $\{\tilde{W}(n), n \in \mathbb{N}_0\}$ defining the eigenvalues of a self-adjoint positive bounded operator $\tilde{\mathcal{W}}$, such that, for certain $m_{\tilde{\mathcal{W}}} > 0, M_{\tilde{\mathcal{W}}} > 0$

$$m_{\tilde{\mathcal{W}}} \leq \left\| \tilde{\mathcal{W}}^{1/2}(\psi) \right\|_{L^2(\mathbb{M}_d, dv; \mathbb{C})}^2 \leq M_{\tilde{\mathcal{W}}}, \quad \psi \in L^2(\mathbb{M}_d, dv; \mathbb{C}); \quad \|\psi\|_{L^2(\mathbb{M}_d, dv; \mathbb{C})} = 1.$$

Under **Condition C1**, define the normalizing self-adjoint integral operator \mathcal{N}_θ by the kernel

$$\begin{aligned} \mathcal{K}_{\mathcal{N}_\theta}(\mathbf{x}, \mathbf{y}) &= \sum_{n \in \mathbb{N}_0} \tilde{W}(n) \left[\int_{-\pi}^{\pi} \frac{B_n^\eta(0) M_n(\omega) [4(\sin(\omega/2))^2]^{-\alpha(n,\theta)/2}}{|\omega|^{-\gamma}} d\omega \right] \\ &\times \sum_{j=1}^{\delta(n,d)} S_{n,j}^d(\mathbf{x}) S_{n,j}^d(\mathbf{y}), \quad \mathbf{x}, \mathbf{y} \in \mathbb{M}_d, \theta \in \Theta, \quad \gamma > 0. \end{aligned} \tag{3.9}$$

Hence, for each $\theta \in \Theta$, and $\omega \in [-\pi, \pi], \omega \neq 0$, the kernel $\mathcal{K}_{\mathcal{Y}_{\omega,\theta}}$ of the density operator

$$\mathcal{Y}_{\omega,\theta} = [\mathcal{N}_\theta]^{-1} \mathcal{F}_{\omega,\theta} = \mathcal{F}_{\omega,\theta} [\mathcal{N}_\theta]^{-1} \tag{3.10}$$

satisfies $\int_{-\pi}^{\pi} \int_{\mathbb{M}_d} \mathcal{K}_{\mathcal{Y}_{\omega,\theta}}(\mathbf{x}, \mathbf{y}) \mathcal{K}_{\mathcal{W}_\omega}(\mathbf{y}, \mathbf{z}) dv(\mathbf{y}) d\omega = \delta(\mathbf{x} - \mathbf{z})$, for $\mathbf{x}, \mathbf{z} \in \mathbb{M}_d$, in the weak sense, meaning that, for every $\varrho, \psi \in L^2(\mathbb{M}_d, dv; \mathbb{C})$,

$$\int_{-\pi}^{\pi} \mathcal{Y}_{\omega,\theta} \mathcal{W}_\omega(\varrho)(\psi) d\omega = \langle \varrho, \psi \rangle_{L^2(\mathbb{M}_d, dv; \mathbb{C})}, \quad \forall \theta \in \Theta. \tag{3.11}$$

Here, $\delta(\mathbf{x} - \mathbf{y})$ denotes the Dirac Delta distribution. Equivalently, $\int_{-\pi}^{\pi} \mathcal{Y}_{\omega,\theta} \mathcal{W}_\omega d\omega$ defines the identity operator $\mathcal{I}_{L^2(\mathbb{M}_d, dv; \mathbb{C})}$ on $L^2(\mathbb{M}_d, dv; \mathbb{C})$ for all $\theta \in \Theta$, having unitary eigenvalues, i.e., $\int_{-\pi}^{\pi} \mathcal{Y}(\omega, n, \theta) W(n, \omega, \gamma) d\omega = 1$, for $n \in \mathbb{N}_0, \theta \in \Theta$.

Given the candidate set constituted by the parametric operator families $\{\Upsilon_{\omega, \theta}, \omega \in [-\pi, \pi]\}$, $\theta \in \Theta$, the theoretical loss function $L(\theta_0, \theta)$ to be minimized is defined as

$$\begin{aligned} L(\theta_0, \theta) &:= \|U_\theta - U_{\theta_0}\|_{\mathcal{L}(L^2(\mathbb{M}_d, dv; \mathbb{C}))} \\ &= \left\| \int_{-\pi}^\pi \mathcal{F}_{\omega, \theta_0} \ln \left(\Upsilon_{\omega, \theta_0} \Upsilon_{\omega, \theta}^{-1} \right) \mathcal{W}_\omega d\omega \right\|_{\mathcal{L}(L^2(\mathbb{M}_d, dv; \mathbb{C}))} \\ &= \left\{ \sup_{n \geq 0} \left| \tilde{W}(n) \int_{-\pi}^\pi \frac{f_{n, \theta_0}(\omega)}{|\omega|^{-\gamma}} \ln \left(\frac{\Upsilon(\omega, n, \theta_0)}{\Upsilon(\omega, n, \theta)} \right) d\omega \right| \right\}, \end{aligned} \tag{3.12}$$

where the theoretical contrast operator U_θ has kernel

$$\begin{aligned} \mathcal{K}_{U_\theta}(\mathbf{x}, \mathbf{y}) &= - \sum_{n \in \mathbb{N}_0} U_\theta(n) \left[\sum_{j=1}^{\delta(n, d)} S_{n, j}^d(\mathbf{x}) S_{n, j}^d(\mathbf{y}) \right] \\ &= - \sum_{n \in \mathbb{N}_0} \left[\sum_{j=1}^{\delta(n, d)} S_{n, j}^d(\mathbf{x}) S_{n, j}^d(\mathbf{y}) \right] \int_{-\pi}^\pi \frac{B_n^n(0) M_n(\omega)}{[4(\sin(\omega/2))^2]^{\alpha(n, \theta_0)/2}} \\ &\quad \times \ln(\Upsilon(\omega, n, \theta)) |\omega|^\gamma \tilde{W}(n) d\omega, \quad \mathbf{x}, \mathbf{y} \in \mathbb{M}_d, \quad \theta \in \Theta. \end{aligned}$$

Hence, $U_\theta \in \mathcal{L}(L^2(\mathbb{M}_d, dv; \mathbb{C}))$ (see also Remark 7 in Ruiz-Medina (2022)).

For every $\theta \in \Theta$, the eigenvalues $\{L_n(\theta_0, \theta), n \in \mathbb{N}_0\}$ of the loss operator $U_\theta - U_{\theta_0}$ satisfy $L_n(\theta_0, \theta) = \tilde{W}(n) \int_{-\pi}^\pi \frac{f_{n, \theta_0}(\omega)}{|\omega|^{-\gamma}} \ln \left(\frac{\Upsilon(\omega, n, \theta_0)}{\Upsilon(\omega, n, \theta)} \right) d\omega \geq 0$ (see Ruiz-Medina (2022) for more details). Hence,

$$\begin{aligned} L(\theta_0, \theta) &= \sup_{n \geq 0} L_n(\theta_0, \theta) > 0, \quad \theta \neq \theta_0 \\ L(\theta_0, \theta) &= \sup_{n \geq 0} L_n(\theta_0, \theta) = 0 \Leftrightarrow \theta = \theta_0. \end{aligned} \tag{3.13}$$

From (3.13),

$$\theta_0 = \arg \min_{\theta \in \Theta} \sup_{n \geq 0} L_n(\theta_0, \theta) = \arg \min_{\theta \in \Theta} \sup_{n \geq 0} U_\theta(n). \tag{3.14}$$

The empirical contrast operator $U_{T, \theta}$

$$U_{T, \theta} = - \int_{-\pi}^\pi p_\omega^{(T)} \ln(\Upsilon_{\omega, \theta}) \mathcal{W}_\omega d\omega, \quad \theta \in \Theta, \tag{3.15}$$

then provides the empirical loss function, and $\widehat{\theta}_T$ can be computed as

$$\widehat{\theta}_T = \arg \min_{\theta \in \Theta} \left\| - \int_{-\pi}^\pi p_\omega^{(T)} \ln(\Upsilon_{\omega, \theta}) \mathcal{W}_\omega d\omega \right\|_{\mathcal{L}(L^2(\mathbb{M}_d, dv; \mathbb{C}))}. \tag{3.16}$$

The following result provides weak-consistency of the minimum contrast parameter estimator $\mathcal{A}_{\hat{\theta}_T}$ of the long-memory operator.

Theorem 2 *Let $\{\tilde{X}_t, t \in \mathbb{Z}\}$ be a Gaussian $L^2(\mathbb{M}_d, dv)$ -valued sequence satisfying **Conditions C0–C1**, as well as the conditions imposed through Eqs. (3.8)–(3.11) with $\gamma > 1$. Assume that the slowly varying functions $M_n(\omega)$, $\omega \in [-\pi, \pi]$, $n \in \mathbb{N}_0$ in Eq. (3.5) are such that, for any $\xi > 0$, $\lim_{\omega \rightarrow 0} \left[\sup_{n \in \mathbb{N}_0} \left| \frac{M_n(\omega/\xi)}{M_n(\omega)} - 1 \right| \right] = 0$. Then, the following limit holds:*

$$E \left\| \int_{-\pi}^{\pi} \left[p_{\omega}^{(T)} - \mathcal{F}_{\omega, \theta_0} \right] \mathcal{W}_{\omega, \theta} d\omega \right\|_{\mathcal{S}(L^2(\mathbb{M}_d, dv; \mathbb{C}))} \rightarrow 0, \quad T \rightarrow \infty, \quad (3.17)$$

where, for $(\omega, \theta) \in [-\pi, \pi] \setminus \{0\} \times \Theta$, $\mathcal{W}_{\omega, \theta} = \ln(\Upsilon_{\omega, \theta}) \mathcal{W}_{\omega}$. The minimum contrast estimator (3.16) then satisfies $\hat{\theta}_T \rightarrow_p \theta_0$, as $T \rightarrow \infty$, where \rightarrow_p denotes convergence in probability.

Proof The proof follows as in Theorem 2 in Ruiz-Medina (2022). \square

Global analysis. Condition (3.1) is a key condition in our approach, leading to Eq. (3.3) introducing the Hilbert–Schmidt operator setting, usually considered in functional time series analysis. Note that, under this setting, LRD still can be displayed (see Eq. (3.7)). Furthermore, Eq. (3.3) allows to apply the spectral analysis of LRD functional time series introduced in Ruiz-Medina (2022) for inference on manifold cross-time RFs. Specifically, Eq. (3.1) ensures Lemma 1 in Ruiz-Medina (2022) holds under alternative conditions for this RF family. Then, asymptotic unbiasedness of the integrated periodogram also holds, beyond the Gaussian scenario under non-structural assumptions (see Theorem 1). Furthermore, Sect. 3.1, and, in particular, **Condition C1**, provides the semiparametric functional spectral scenario introduced in Ruiz-Medina (2022) to be applied for minimum contrast estimation, when a functional sample of a manifold cross-time RF can be observed. Theorem 2 ensures weak-consistency under a Gaussian scenario as given in Ruiz-Medina (2022).

4 SRD–LRD estimation in the spectral domain

This section has a double, theoretical and practical, motivation. Specifically, on the one hand a wider family of spatiotemporal RF models is analyzed displaying SRD and LRD at different manifold scales, in the spirit of the LRD framework introduced in Li et al. (2019), but extended to the multifractional context. On the other hand, this manifold-scale varying memory behavior can be observed in some stochastic fractional or multifractional pseudodifferential in time evolution equations, defined from a local spatial differential operator, where the decay velocity of the temporal correlation function is accelerated by the decay of the spatial pure point spectrum, modifying the temporal LRD level of the model at the smallest spatial scales. The reverse situation can be observed in processes defined by evolution equations given by a local differential operator in time, and a fractional or multifractional pseudodifferential

operator in space. Thus, the solution to these models displays a spatial fractal behavior, reflected in a slow decay of its spatial pure point spectrum, slowing down the decay velocity of the temporal correlation function, leading to a stronger dependence at small spatial scales. Both behaviors can be observed within the model family introduced in Anh et al. (2018), Anh et al. (2016a); Anh et al. (2016b).

Let us now consider in **Condition C1**, $l_\alpha(\theta) = 0$, and $\alpha(n, \theta) = 0$, for $n \in \mathcal{D}_{\text{SRD}} \subset \mathbb{N}_0$, meaning that the process projected into the eigenspaces H_n , $n \in \mathcal{D}_{\text{SRD}} \subset \mathbb{N}_0$, of the spherical Laplace Beltrami operator displays SRD. While LRD is observed at the remaining eigenspaces. Without loss of generality let $\mathcal{D}_{\text{SRD}} = \{0, \dots, n_0\}$, for certain $n_0 \geq 1$. (The reverse situation where the eigenvalues of the LRD operator vanish at large n has been analyzed in the simulation study in Sect. 5.2). The projected SRD process then admits the following expansion (see Theorem 1 in the Supplementary Material):

$$\tilde{X}_t^{(n_0)}(\mathbf{x}) = \sum_{n=0}^{n_0} \sum_{j=1}^{\delta(n,d)} V_{n,j}(t) S_{n,j}^d(\mathbf{x}), \quad \mathbf{x} \in \mathbb{M}_d, \quad t = 1, \dots, T.$$

For $\omega \in [-\pi, \pi]$, the fDFT projected into $\oplus_{n=0}^{n_0} H_n$ is expressed as

$$\tilde{X}_\omega^{(T,n_0)}(\mathbf{x}) = \sum_{n=0}^{n_0} \sum_{j=1}^{\delta(n,d)} \left[\frac{1}{\sqrt{2\pi T}} \sum_{t=1}^T V_{n,j}(t) \exp(-i\omega t) \right] S_{n,j}^d(\mathbf{x}), \quad \mathbf{x} \in \mathbb{M}_d.$$

The corresponding projected periodogram operator $p_\omega^{(T,n_0)} = \tilde{X}_\omega^{(T,n_0)} \otimes \overline{\tilde{X}_\omega^{(T,n_0)}}$ then involves the tensorial product of the eigenfunctions of the Laplace Beltrami operator up to order n_0 . For $\omega \in [-\pi, \pi]$, the kernel estimator

$$\hat{f}_\omega^{(T,n_0)}(\mathbf{x}, \mathbf{y}) = \left[\frac{2\pi}{T} \right] \sum_{t \in [1, T-1]} W^{(T)} \left(\omega - \frac{2\pi t}{T} \right) p_{2\pi t/T}^{(T,n_0)}(\mathbf{x}, \mathbf{y}), \quad \mathbf{x}, \mathbf{y} \in \mathbb{M}_d,$$

of \mathcal{F}_ω projected into $\oplus_{n=0}^{n_0} H_n$, based on the weighted periodogram operator, is computed. Here, $W^{(T)}(x) = \sum_{j \in \mathbb{Z}} \frac{1}{B_T} W \left(\frac{x+2\pi j}{B_T} \right)$, with B_T being the positive bandwidth parameter. Function W on \mathbb{R} is real, and such that W is positive, even, and bounded in variation, with $W(x) = 0$ if $|x| \geq 1$, $\int_{\mathbb{R}} |W(x)|^2 dx < \infty$, and $\int_{\mathbb{R}} W(x) dx = 1$ (see Panaretos and Tavakoli (2013a)).

Under **Condition C1**, the minimum contrast estimators $\hat{\alpha}_T(n, \theta_0) = \alpha(n, \hat{\theta}_T)$, $n > n_0$, are computed as given in Eqs. (3.8)–(3.16). Hence, the mixed SRD–LRD kernel estimator of the spectral density operator is given by

$$\begin{aligned} \hat{f}_\omega^{(T)}(\mathbf{x}, \mathbf{y}) &= \hat{f}_\omega^{(T,n_0)}(\mathbf{x}, \mathbf{y}) + \hat{f}_\omega^{(T,(n_0+1,\infty))}(\mathbf{x}, \mathbf{y}, \hat{\theta}_T) \\ &= \left[\frac{2\pi}{T} \right] \sum_{t \in [1, T-1]} W^{(T)} \left(\omega - \frac{2\pi t}{T} \right) p_{2\pi t/T}^{(T,n_0)}(\mathbf{x}, \mathbf{y}) \end{aligned}$$

$$+ \sum_{n=n_0+1}^{\infty} \frac{B_n^\eta(0)M_n(\omega)}{[4(\sin(\omega/2))^2]^{\alpha(n,\theta_T)/2}} \sum_{j=1}^{\delta(n,d)} S_{n,j}^d(\mathbf{x})S_{n,j}^d(\mathbf{y}). \tag{4.1}$$

5 Simulation study

This section illustrates the results derived in the context of multifractionally integrated SPHARMA(p,q) processes (see, e.g., Example 1 in Sect. 3.3 in Ruiz-Medina (2022), and Li et al. (2019) in the particular case of fractionally integrated functional autoregressive moving averages processes). See also Caponera et al. (2022) and Caponera and Marinucci (2021) for the case of SPHARMA(p,q) processes.

Considering the unit sphere \mathbb{S}_2 in \mathbb{R}^3 , and hence, the separable Hilbert space $H = L^2(\mathbb{S}_2, d\nu)$, a multifractionally integrated SPHARMA(p,q) process $\{\tilde{X}_t, t \in \mathbb{Z}\}$ is defined by the following state space equation:

$$(\mathcal{I}_{L^2(\mathbb{S}_2, d\nu)} - B)^{\mathcal{A}_\theta/2}(\Phi_p(B)\tilde{X}_t)(\mathbf{x}) = \varepsilon_t(\mathbf{x}) + (\Psi_q(B)\varepsilon_t)(\mathbf{x}), \quad \mathbf{x} \in \mathbb{S}_2, t \in \mathbb{Z}. \tag{5.1}$$

Condition C1 holds, since this model constitutes a particular case $H = L^2(\mathbb{S}_2, d\nu)$ of the more general formulation given in Sect. 3.3 in Ruiz-Medina (2022) in the functional time series framework. Then, as before, \mathcal{A}_θ is the LRD operator satisfying $l_\alpha(\theta), L_\alpha(\theta) \in (0, 1/2)$. In particular, Eq. (3.7) holds. Here, operator $(\mathcal{I}_{L^2(\mathbb{S}_2, d\nu)} - B)^{\mathcal{A}_\theta/2}$ is interpreted as in Characiejus and Răckauskas (2014), Răckauskas and Suquet (2011), and B is a difference operator satisfying $E\|B^j\tilde{X}_t - \tilde{X}_{t-j}\|_H^2 = 0$, for $t, j \in \mathbb{Z}$.

Here, $\Phi_p(B) = 1 - \sum_{k=1}^p \Phi_k B^k$, and $\Psi_q(B) = \sum_{l=1}^q \Psi_l B^l$, where operators $\Phi_k, k = 1, \dots, p$, and $\Psi_l, l = 1, \dots, q$, are assumed to be invariant positive self-adjoint bounded operators on $L^2(\mathbb{S}_2, d\nu)$ admitting the representation:

$$\begin{aligned} \Phi_k &= \sum_{n \in \mathbb{N}_0} \lambda_n(\Phi_k) \sum_{j=1}^{\delta(n,d)} S_{n,j}^d \otimes S_{n,j}^d, \quad k = 1, \dots, p \\ \Psi_l &= \sum_{n \in \mathbb{N}_0} \lambda_n(\Psi_l) \sum_{j=1}^{\delta(n,d)} S_{n,j}^d \otimes S_{n,j}^d, \quad l = 1, \dots, q. \end{aligned} \tag{5.2}$$

Here, $d = 2, \delta(n, 2) = 2n + 1, \mathbb{M}_2 = \mathbb{S}_2, \omega_2 = |\mathbb{S}_2| = 4\pi$. Also, $\Phi_{p,n}(z) = 1 - \sum_{k=1}^p \lambda_n(\Phi_k)z^k$ and $\Psi_{q,n}(z) = \sum_{l=1}^q \lambda_n(\Psi_l)z^l, n \in \mathbb{N}_0$, have not common roots, and their roots are outside of the unit circle (see Corollary 6.17 in Beran (2017)). By similar arguments, as justified in Sects. 3.3 and 6 in Ruiz-Medina (2022), conditions (3.8)–(3.11) are satisfied by this model family. Hence, the results given in Theorems 1 and 2 hold.

Theorem 1 and Sect. 1.1 of the Supplementary Material have been applied in the simulation methodology adopted in the generations of some special cases within the family of multifractionally integrated SPHARMA(p,q) processes. In particular,

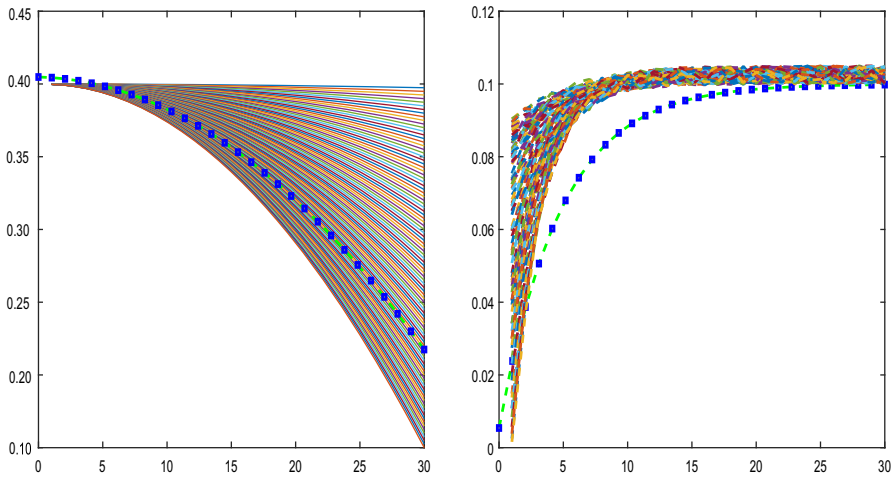


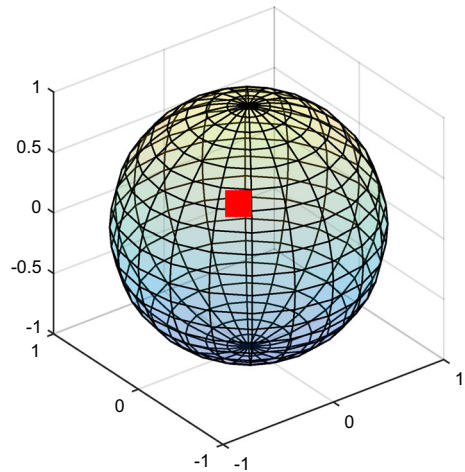
Fig. 1 The first 30 eigenvalues $\alpha(n, \theta_0)$, $n = 1, \dots, 30$ of the LRD operator \mathcal{A}_{θ_0} (dotted blue–green line), and the set of 100 parametric candidates $\alpha(n, \theta_i)$, $n = 1, \dots, 30$, $i = 1, \dots, 100$, for decreasing LRD operator eigenvalues (left–hand side). The first 30 eigenvalues $\alpha(n, \vartheta_0)$, $n = 1, \dots, 30$ (dotted blue–green line) of the LRD operator $\mathcal{A}_{\vartheta_0}$, and the set of 100 parametric candidates $\alpha(n, \vartheta_i)$, $n = 1, \dots, 30$, $i = 1, \dots, 100$, for increasing LRD operator eigenvalues (right–hand side)

a spherical uniform pole $\mathbf{U} = \mathbf{u}_0$ (see Fig. 2) in the involved zonal functions (defined from the Legendre polynomials $\{P_n, n \in \mathbb{N}_0\}$) has been independently generated of the $L^2(\mathbb{S}_2, d\nu)$ -valued Gaussian strong–white noise innovation process with variance $\sigma_\varepsilon^2 = \sum_{n \in \mathbb{N}_0} [\sigma_n^\varepsilon]^2$. Table 3 of the Supplementary Material provides the specific parametric scenarios considered. Under such scenarios, Sect. 3 of the Supplementary Material displays generations of some special cases of multifractionally integrated SPHARMA(p,q) processes, for $p = 1, 3$ and $q = 0$, and $p = 1, 3$, and $q = 1$ in Eq. (5.1). The particular cases analyzed of LRD operator eigenvalue sequences can be found in Table 1 of the Supplementary Material. In the implementation of the minimum contrast estimation methodology, we consider 100 candidate systems of parametric eigenvalues for the LRD operator (see Table 2 in the Supplementary Material). These candidate sets are displayed in Fig. 1 jointly with the true eigenvalue sequence.

The functional spherical values at different times of the generated multifractionally integrated SPHAR(3) process are displayed for $M = 10$ under decreasing eigenvalue sequence of the LRD operator in Fig. 3. As commented, the remaining special cases are plotted in Sect. 3 of the Supplementary Material. Additionally, generations under LRD operator with eigenvalues vanishing for $n \geq n_0 = 16$, i.e., the LRD–SRD case, is shown in Sect. 3.1 of the Supplementary Material for multifractionally integrated SPHARMA(1,1) process.

It can be observed in all generations, displayed on a spherical angular neighborhood of the selected pole (see Fig. 2), that persistent in time of the local spherical behavior is stronger when a positive bounded non-decreasing sequence of eigenvalues of LRD operator is considered, since the highest positive eigenvalues are displayed at high discrete Legendre frequencies. For decreasing eigenvalue sequence of the LRD operator,

Fig. 2 The selected pole in the zonal functions



the opposite LRD effect is observed through spherical scales. One can also observe a symmetry in the evolution in time of the spherical patterns, under both, decreasing and increasing LRD operator eigenvalue sequences, when spatial spherical SRD is observed. An increasing level of local linear correlation in space at intermediate times is displayed when autoregression of order 3 is considered.

5.1 Minimum contrast estimation results

We now display the minimum contrast estimation results referred to the multifractionally integrated SPHAR(3) process, when LRD operator \mathcal{A}_θ has decreasing sequence of eigenvalues as plotted at the left-hand side of Fig. 1, under a truncation order $M = 30$. See Sect. 4 of the Supplementary Material, for the remaining cases of multifractionally integrated SPHAR(1), SPHAR(3), SPHARMA(1,1), SPHARMA(3,1) processes. Specifically, Fig. 4 displays, for $i = 1, \dots, 100$ frequency nodes, operator $|\mathcal{M}_{\omega_i}|^{1/2}$ (left-hand side), and $|4(\sin(\omega_i/2))^2|^{-\mathcal{A}_\theta/4} |\mathcal{M}_{\omega_i}|^{1/2}$ (right-hand side), projected into H_n , $n = 1, \dots, 30$. These factors have been computed in the implementation of the minimum contrast estimation methodology in the functional spectral domain. Figure 5 provides the projected spectral density operator kernel at temporal Fourier frequencies $\omega = -\pi + 0.0628(10)i$, $i = 1, 3, 7, 10$ in the interval $[-\pi, \pi]$. Its empirical counterpart is given in Fig. 6 where the modulus of the projected fDFT, and tapered periodogram operator kernel of the generated data at temporal Fourier frequency zero are displayed. The last one over a grid of 30×30 Legendre frequencies. The projected empirical contrast operator $\mathbf{U}_{T,\theta}$ in Eq. (3.15) is then computed. Its minimization is performed in the bounded operator norm.

Under the LRD operator scenario plotted at the left-hand side of Fig. 1 (see also Table 1 of the Supplementary Material), Fig. 7 displays the histograms of the temporal mean of the empirical absolute errors from $R = 100, 2000, 5000$ independent generations of a functional sample of size $T = 1000$ of multifractionally integrated SPHAR(3) process. The empirical analysis performed for the remaining cases under

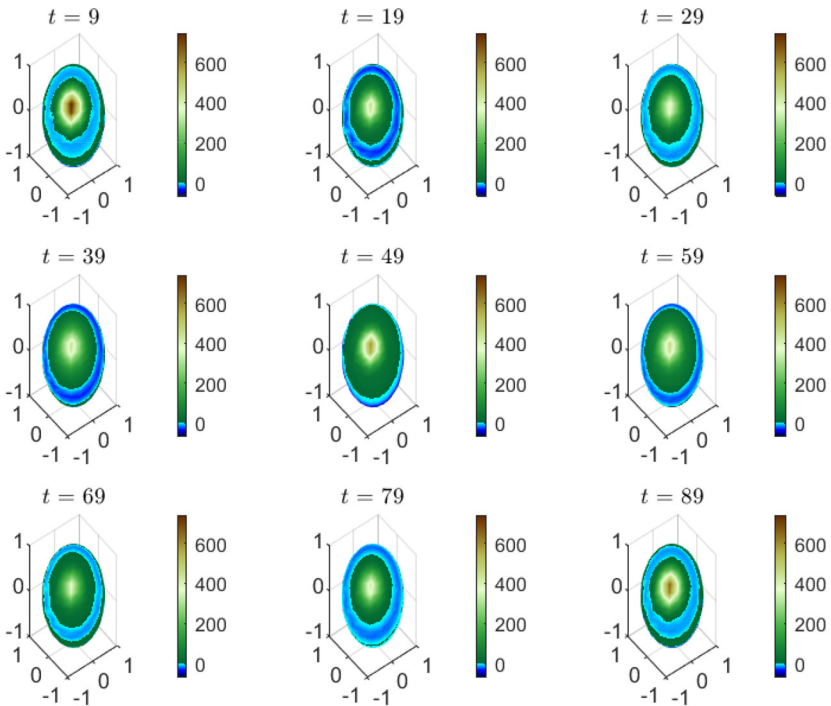


Fig. 3 Generations of multifractionally integrated SPHAR(3) process \tilde{X} at times $t = 9, 19, 29, 39, 49, 59, 69, 79, 89$, projected into the direct sum $\oplus_{n=1}^{10} H_n$ of eigenspaces of the spherical Laplace Beltrami operator on $L^2(\mathbb{S}_2, d\nu)$ under decreasing eigenvalue sequence of the LRD operator

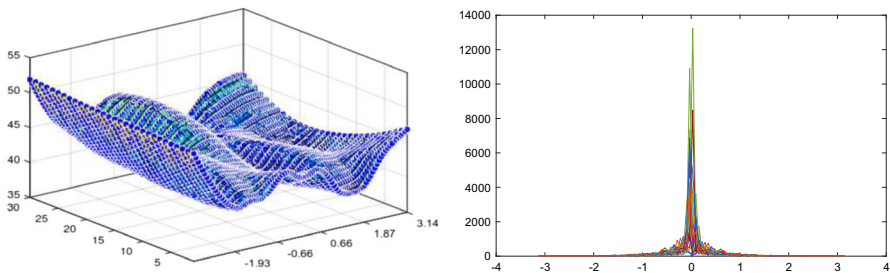


Fig. 4 The square root (s.r.) of the modulus of the projected regular factor of the spectral density operator (left-hand side), and the product of this factor with the s.r. of the modulus of the singular factor of the spectral density operator (right-hand side) at Legendre frequencies $n = 1, \dots, 30$

decreasing LRD operator eigenvalue sequence, from $R = 100, 2000, 5000$ independent generations of each one of the functional samples of size $T = 50, 500, 1000$ considered, are given in Sects. 4.1, 4.3, 4.5, and 4.7 of the Supplementary Material (see also Sects. 4.2, 4.4, 4.6 and 4.8 of the Supplementary Material for the same analysis under increasing LRD operator eigenvalue sequence as plotted at the right-hand side of Fig. 1). The results are displayed for the eigenspaces $H_n, n = 1, 5, 10, 15, 20, 25, 30$.

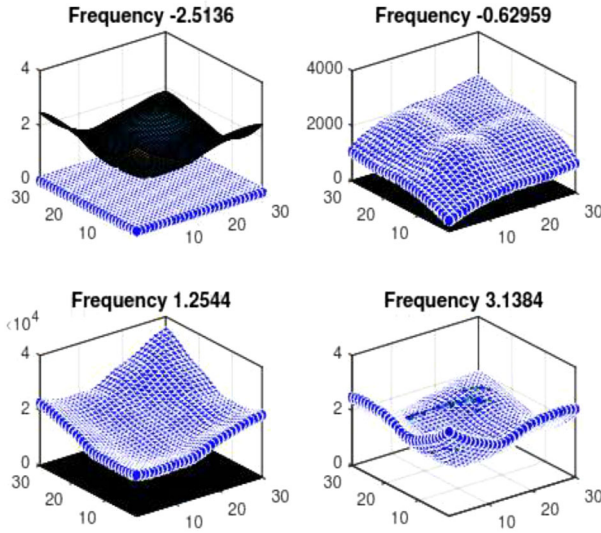


Fig. 5 Kernel of spectral density operator $\mathcal{F}_{\omega, \theta_0}$ projected into $H_n \otimes H_n$, $n = 1, \dots, 30$, for temporal Fourier frequencies $\omega = -\pi + 0.0628(10)i$, $i = 1, 3, 7, 10$

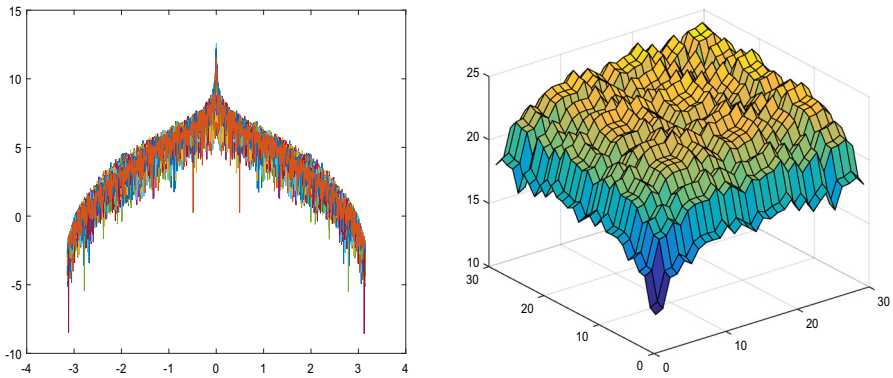


Fig. 6 The modulus of the projected fDFT of the data, 30 spectral curves corresponding to 30 discrete Legendre frequencies (left-hand side). Tapered periodogram kernel at zero temporal Fourier frequency over a 30×30 grid of discrete Legendre frequencies (right-hand side). Both, fDFT and tapered periodogram kernel, are displayed at the logarithm scale

The empirical probabilities

$$\widehat{P} \left(\|f_{n, \theta_0}(\cdot) - f_{n, \widehat{\theta}_T}(\cdot)\|_{L^1([-\pi, \pi])} > \varepsilon_i \right), \quad i = 1, \dots, 100, \tag{5.3}$$

are computed under decreasing and increasing LRD operator eigenvalue sequence, for the multifractionally integrated SPHAR(3) model in Fig. 8, considering $R = 100, 2000, 5000$ independent generations of each one of the functional samples of size $T = 50, 500, 1000$. In all scenarios displayed in Sect. 4 of the Supplementary Material, the empirical probabilities (5.3) are computed from projection into the

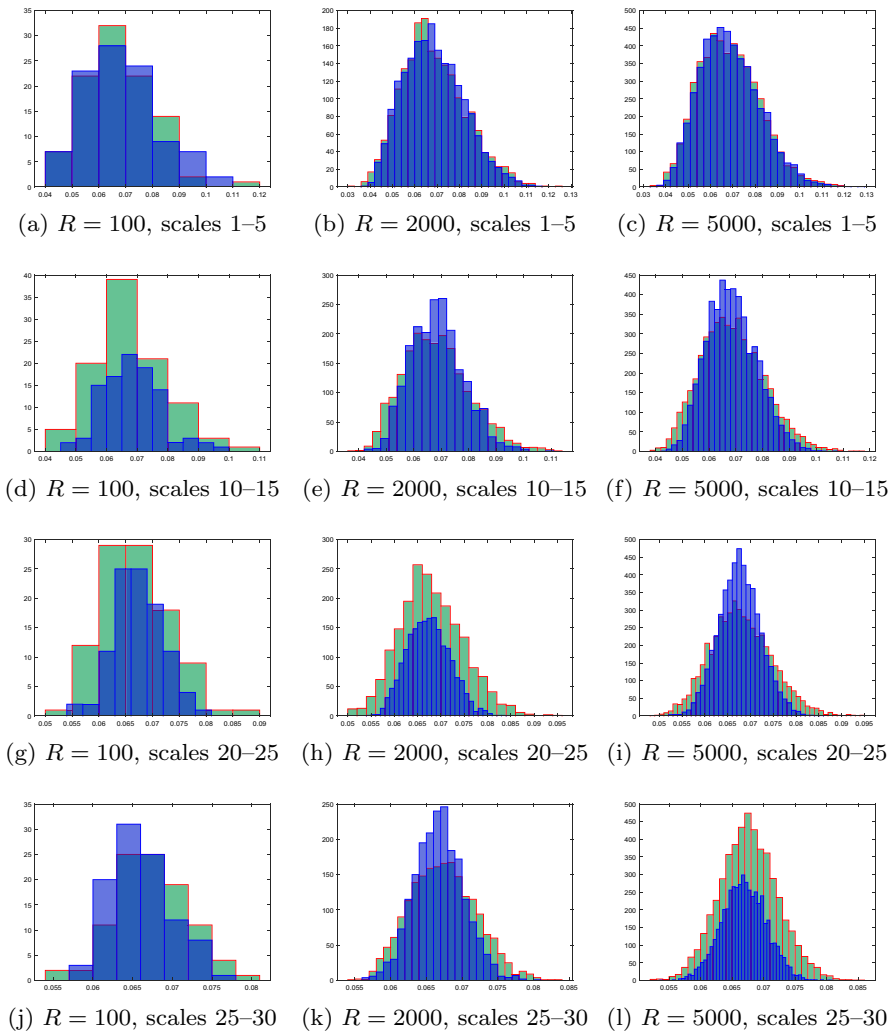


Fig. 7 Histograms of the temporal mean of the empirical absolute errors from a functional sample of size $T = 1000$ (LRD operator decreasing eigenvalue sequence)

eigenspaces H_n , $n = 1, \dots, 30$ of the Laplace Beltrami operator, and for a grid of 100 thresholds in the interval $(0, 0.1)$.

When the number of repetitions increases, the tails of the empirical distribution of the temporal mean of the empirical absolute errors become lighter, being the shape of the empirical distribution closer to a Gaussian distribution. This effect associated with the increasing of the sample size is more pronounced at highest spatial resolution levels (i.e., at high discrete Legendre frequencies). In particular, the empirical distribution of the temporal mean of the empirical absolute errors becomes more concentrated around its mean faster at higher than at coarser resolution levels. A similar behavior is observed in the asymmetric empirical distribution of quadratic error temporal mean,

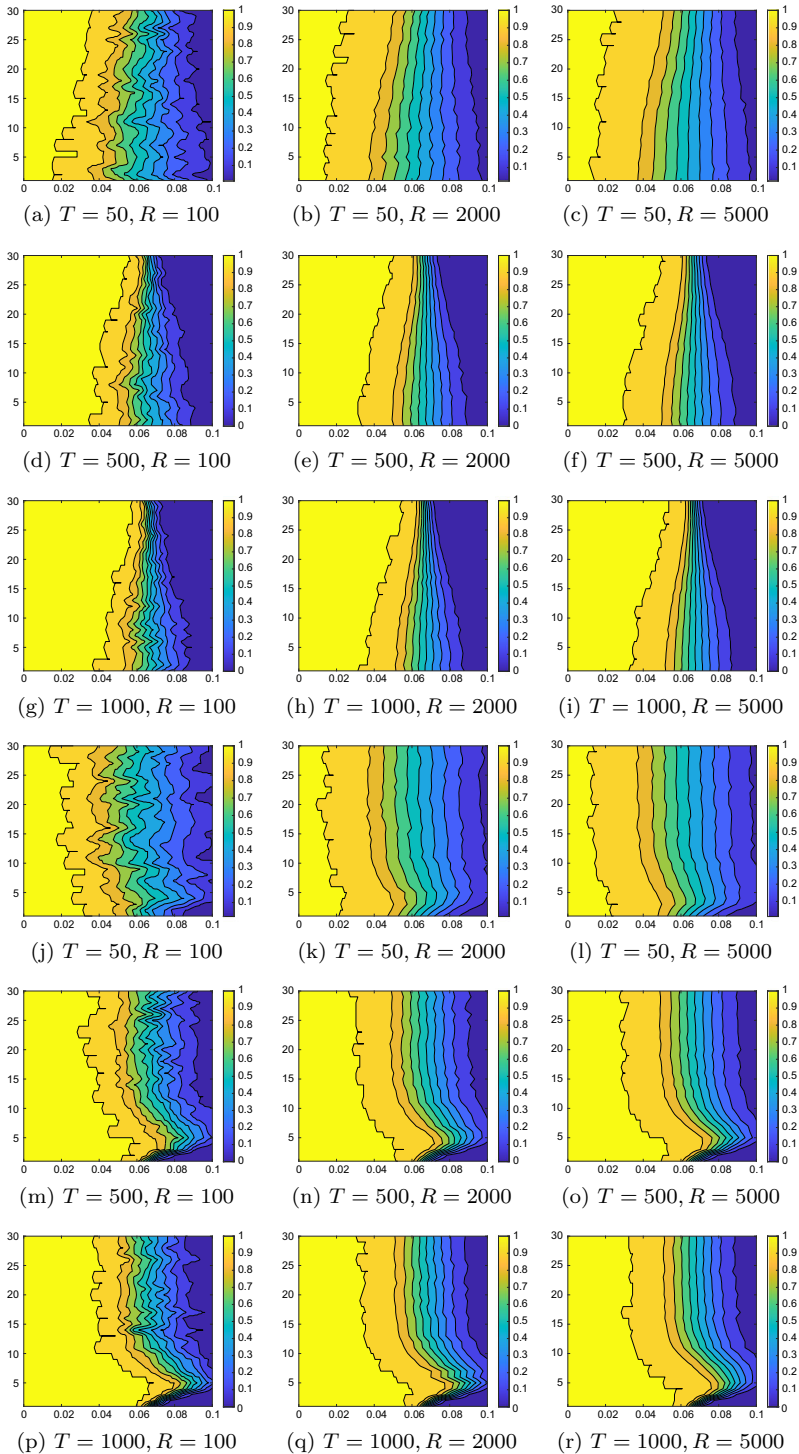
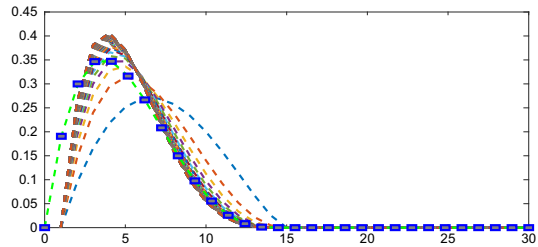


Fig. 8 Empirical probabilities in Eq. (5.3), LRD operator decreasing eigenvalue sequence (plots a–i), and LRD operator increasing eigenvalue sequence (plots j–r)

Fig. 9 Eigenvalues of \mathcal{A}_{θ_0} for the case of SRD–LRD models (dotted blue–green line), and the eigenvalues of the 100 parametric candidates \mathcal{A}_{θ_i} , $i = 1, \dots, 100$, considered



displaying a larger degree of dispersion, due to the stronger effect of the functional spectral singularity at zero frequency.

Regarding the empirical probability analysis, one can observe that the increasing of R has a strong effect by spherical scales on the gradually decay of the empirical probabilities to zero over the smallest threshold values in the grid in the interval $(0, 0.1)$, while increasing parameter T enlarges the dark blue area, in the contour plots displayed, where empirical probabilities become zero over the largest threshold values in the grid analyzed. Note that the opposite effects of parameter R by spherical scales, in the increasing and decreasing LRD operator eigenvalue scenarios, are observed. All the results displayed are affected by a numerical integration error.

5.2 SRD–LRD estimation results

In this section, we study the case where the projected spherical functional process displays LRD at discrete Legendre frequencies $n = 1, \dots, 15$, while SRD is observed at discrete Legendre frequencies $n = 16, \dots, 30$. The eigenvalues $\{\alpha(n, \theta), n = 1, \dots, 15\}$ of \mathcal{A}_θ are displayed for $\theta = \theta_0$ in Fig. 9. The 100 candidate eigenvalue systems $\{\alpha(n, \theta_i), n = 1, \dots, 15, i = 1, \dots, 100\}$, $\theta_i \in \Theta, i = 1, \dots, 100$, involved in the implementation of the minimum contrast estimation procedure are also showed in Fig. 9. These eigenvalue systems are computed from sampling a scaled beta distribution with parameters 2 and $\frac{5i}{i+1}$, $i = 1, \dots, 100$.

For multifractionally integrated SPHARMA(1,1) process, the modulus of the fDFT projected into the eigenspaces $H_n, n = 1, \dots, 15$, of the spherical Laplace Beltrami operator, where LRD is displayed, is showed at the left-hand side of Fig. 10. The modulus of the fDFT projected into the eigenspaces $H_n, n = 16, \dots, 30$, where SRD is displayed, can be found at the right-hand side of Fig. 10. In the last case, its weighted kernel operator estimator, based on the Gaussian kernel and bandwidth parameter $B_T = 0.2$, is given at the right-hand side of Fig. 11. For the minimum contrast parametric estimator $\widehat{f}_\omega^{(T, n_0)}(\cdot, \widehat{\theta}_T)$ with $n_0 = 15$, minimizing over the 100 candidate parametric models the bounded linear operator \mathcal{L} norm ($L^2(\mathbb{S}_2, dv; \mathbb{C})$) of the empirical contrast operator $\mathbf{U}_{T, \theta}$ in (3.15), Fig. 12 displays the empirical probabilities $\widehat{\mathcal{P}}\left(\|f_n(\cdot) - \widehat{f}_n^{(T, n_0)}(\cdot, \widehat{\theta}_T)\|_{L^1([-\pi, \pi])} > \varepsilon_i\right)$, for $n = 1, \dots, 15$, and thresholds $\varepsilon_i = i(0.016) \in (0, 0.8)$, $i = 1, \dots, 50$.

The performance of the SRD–LRD estimation methodology is also analyzed for the remaining multifractionally integrated spherical functional processes generated as

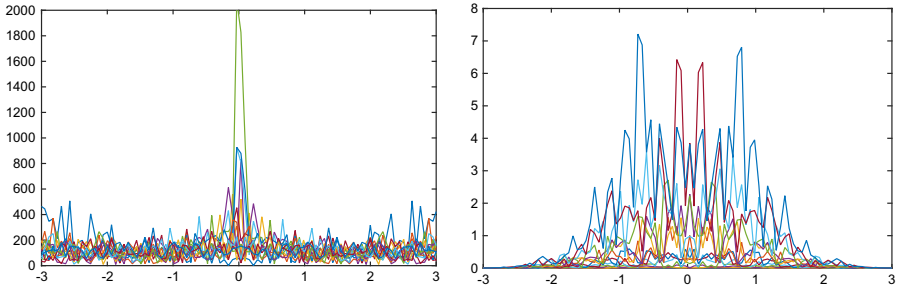


Fig. 10 Modulus of the projected LRD fDFT for discrete Legendre frequencies $n = 1, \dots, 15$ (left-hand side), and modulus of the projected SRD fDFT for discrete Legendre frequencies $n = 16, \dots, 30$ (right-hand side)

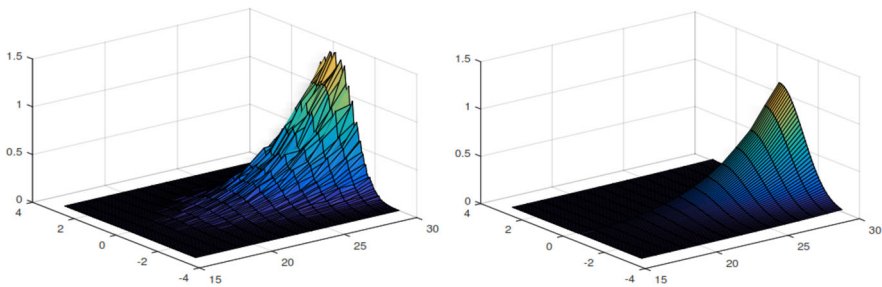


Fig. 11 The modulus of the fDFT projected into the eigenspaces $H_n, n = 16, \dots, 30$, (left-hand side), and its weighted kernel operator estimator (right-hand side)

displayed in Fig. 13. Specifically, in this figure, results in terms of the empirical mean quadratic errors, associated with SRD functional spectral estimation (left hand-side), and in terms of the histograms of the temporal mean of the empirical absolute errors (right hand-side), associated with LRD spectral estimation, are respectively showed from $R = 300$ independent generations of a functional sample of size $T = 500$. Results for $T = 50, T = 100, T = 500, T = 1000$, and $R = 100$ are displayed in Sect. 5 of the Supplementary Material.

One can observe since $T = 500$ the order of magnitude of the empirical mean quadratic errors is 10^{-4} for the bandwidth parameter $B_T = 0.2$ in the SRD estimation. It is well-known that the bandwidth parameter affects precision of the weighted periodogram operator estimator, and the impact of parameter T is very strong. This fact can also be observed in Sect. 5 of the Supplementary Material, looking at differences in the magnitude of empirical mean quadratic errors, based on 100 repetitions, associated with the weighted periodogram operator for $T = 50$ and $T = 100$, considering bandwidth parameter $B_T = 0.1$, as well as for $T = 500$, and $T = 1000$, considering bandwidth parameter $B_T = 0.2$, since a substantial reduction in such magnitudes occurs when increasing the functional sample size T (see, e.g., Theorem 3.6 in Panaretos and Tavakoli (2013a)). Similar results as in previous section are obtained in terms of the empirical distribution of the temporal mean of the empirical

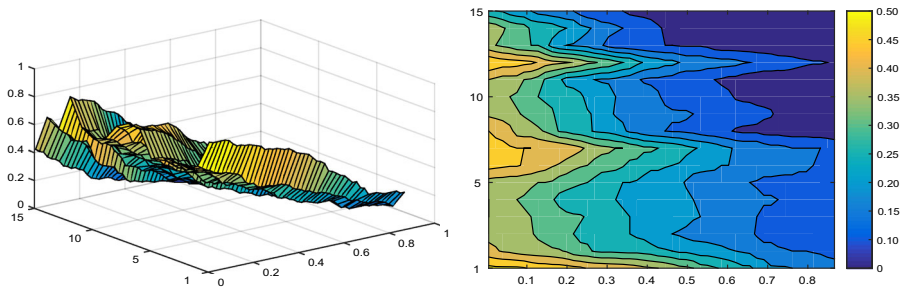


Fig. 12 The empirical probabilities $\widehat{\mathcal{P}}\left(\left\|f_n(\cdot) - \widehat{f}_n(\cdot, \widehat{\theta}_T^{(T, n_0)})\right\|_{L^1([-\pi, \pi])} > \varepsilon_i\right)$, for $n = 1, \dots, 15$, and $\varepsilon_i = i(0.016) \in (0, 0.8)$, $i = 1, \dots, 50$, based on 100 independent generations of a functional sample of size $T = 100$ (surface and contour plot left to right-hand side)

absolute errors in the implementation of minimum contrast estimation methodology for $n = 1, \dots, 15$.

6 Final comments

Results displayed in Sects. 5.1 and 5.2 (see also Sects. 4 and 5 of the Supplementary Material) are based on the computation of the empirical distribution of the temporal mean of the absolute errors, and the empirical probabilities. The interaction between parameters n , R and T in the asymptotic analysis of the two estimation methodologies proposed is illustrated beyond the Gaussian scenario in the simulation study undertaken. Specifically, from the empirical distributions plotted, one can conclude that their rate of convergence is a function of the spherical scale n , the functional sample size T , and the number of repetitions R . Differences between empirical distributions of absolute errors by scales are more pronounced for decreasing sequence of LRD operator eigenvalues than in the case of increasing LRD operator eigenvalue sequence. As expected (see also Supplementary Material), the effect of the element of SPHARMA(p,q) process family considered is negligible for the minimum contrast estimation methodology. Namely, a slightly increasing of the concentration rate of the empirical errors when the parameter of autoregression p increases is observed. Additionally, the empirical probability analysis also reflects the interaction of these three parameters through the rate of converge to zero. Under nondecreasing eigenvalue sequence of the LRD operator, a smoother decay to zero of the empirical probabilities than in the case of decreasing eigenvalue sequence of the LRD operator is observed. A new battery of limit results will be investigated beyond the Gaussian scenario in a subsequent paper for the asymptotic analysis of the proposed estimators of the second-order structure of the LRD manifold cross-time RFs studied here.

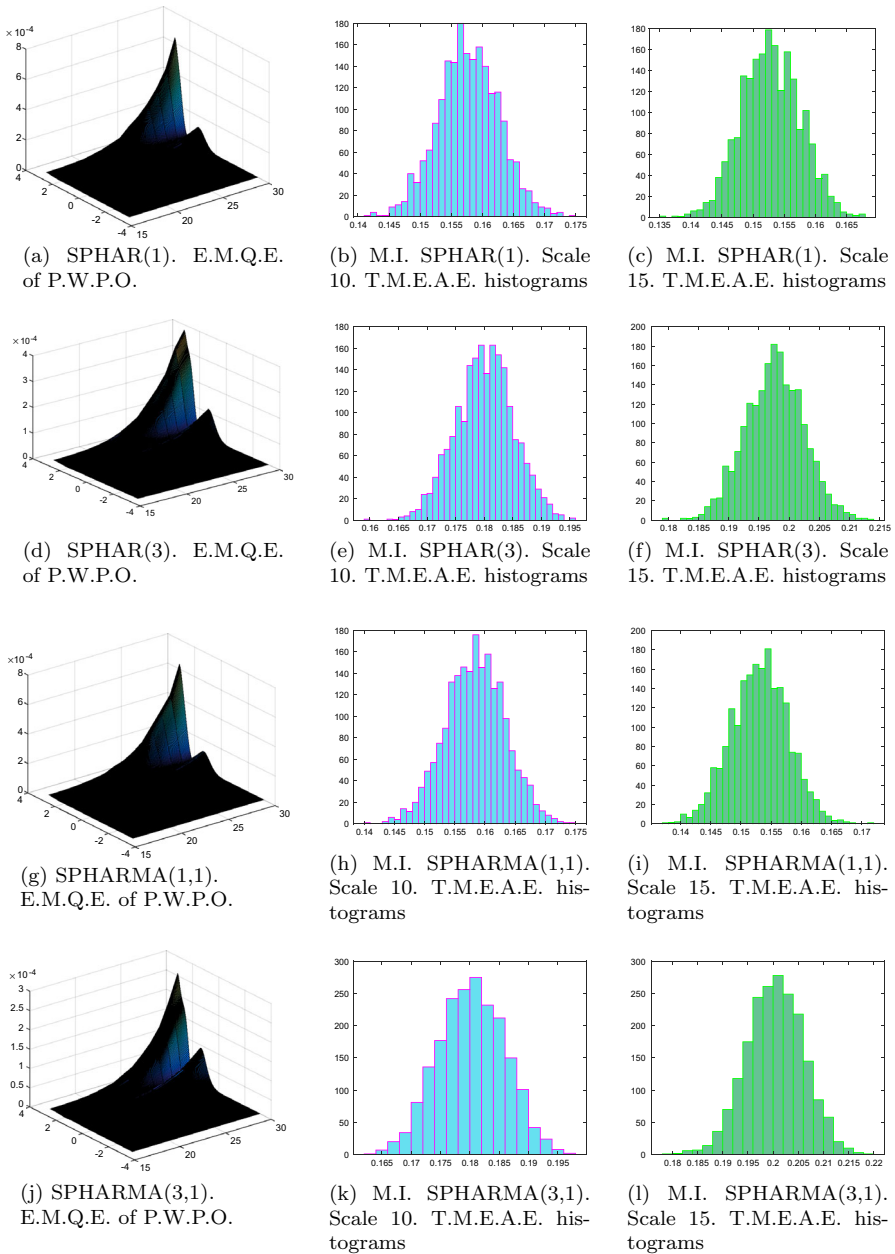


Fig. 13 The empirical mean quadratic errors (E.M.Q.E.s) associated with the projected weighted periodogram operator (P.W.P.O.) estimator (eigenspaces H_n , $n = 16, \dots, 30$, of the Laplace Beltrami operator), are displayed at the left-hand side. The remaining plots provide the histograms of the temporal mean of the empirical absolute errors, associated with the minimum contrast parameter estimation of LRD operator defining multifractional integration (M.I), for eigenspaces H_n , $n = 10, 15$. All the results displayed are based on $R = 300$ independent generations of a functional sample of size $T = 500$. The bandwidth parameter $B_T = 0.2$ has been chosen in all the cases

Supplementary Information The online version contains supplementary material available at <https://doi.org/10.1007/s11749-023-00913-7>.

Acknowledgements This work has been supported in part by projects MCIN/ AEI/PID2022-142900NB-I00, and CEX2020-001105-M MCIN/ AEI/10.13039/501100011033). The authors would like to thank the Editor in Chief and Associate Editor, as well as two anonymous reviewers for their helpful and constructive comments and suggestions which have led to a substantial improvement of this paper.

Funding Funding for open access publishing: Universidad de Granada/CBUA.

Declarations

Conflict of interest The authors declare that they have no conflict of interest.

Open Access This article is licensed under a Creative Commons Attribution 4.0 International License, which permits use, sharing, adaptation, distribution and reproduction in any medium or format, as long as you give appropriate credit to the original author(s) and the source, provide a link to the Creative Commons licence, and indicate if changes were made. The images or other third party material in this article are included in the article's Creative Commons licence, unless indicated otherwise in a credit line to the material. If material is not included in the article's Creative Commons licence and your intended use is not permitted by statutory regulation or exceeds the permitted use, you will need to obtain permission directly from the copyright holder. To view a copy of this licence, visit <http://creativecommons.org/licenses/by/4.0/>.

References

- Alegría A, Bissiri PG, Cleanthous G, Porcu E, White P (2021) Multivariate isotropic random fields on spheres: Nonparametric Bayesian modeling and L_p fast approximations. *Electron J Statist* 15:2360–2392
- Andrews GE, Askey R, Roy R (1999) *Special Functions. Encyclopedia of Mathematics and its Applications. Vol. 71.* Cambridge University Press, Cambridge
- Anh VV, Broadbridge P, Olenko A, Wang YG (2018) On approximation for fractional stochastic partial differential equations on the sphere. *Stoch Environ Res Risk Assess* 32:2585–2603
- Anh V, Leonenko NN, Ruiz-Medina MD (2016) Space-time fractional stochastic equations on regular bounded open domains. *Fract Calc Appl Anal* 19:1161–1199
- Anh V, Leonenko NN, Ruiz-Medina MD (2016) Fractional-in-time and multifractional-in-space stochastic partial differential equations. *Fract Calc Appl Anal* 19:1434–1459
- Beran J (2017) *Mathematical Foundations of Time Series Analysis.* Springer, Switzerland
- Bosq D (2000) *Linear Processes in Function Spaces.* Springer, New York
- Caponera A (2021) SPHARMA approximations for stationary functional time series in the sphere. *Stat Infer Stoch Proc.* 24:609–634
- Caponera A, Fageot J, Simeoni M, Panaretos VM (2022) Functional estimation of anisotropic covariance and autocovariance operators on the sphere. *Electron J Stat* 16:5080–5148
- Caponera A, Marinucci D (2021) Asymptotics for spherical functional autoregressions. *Ann Stat* 49:346–369
- Characiejus V, Räckauskas A (2014) Operator self-similar processes and functional central limit theorems. *Stochastic Process Appl* 124:2605–2627
- Cleanthous G, Georgiadis AG, Lang A, Porcu E (2020) Regularity, continuity and approximation of isotropic Gaussian random fields on compact two-point homogeneous spaces. *Stoch Process their Appl* 130:4873–4891
- Cleanthous G, Porcu E, White P (2021) Regularity and approximation of Gaussian random fields evolving temporally over compact two-point homogeneous spaces. *Test* 30:836–860
- D' Ovidio M, Leonenko NN, Orsingher E, (2016) Fractional spherical random fields. *Statist Probab Lett* 116:146–156
- Giné E (1975) The addition formula for the eigenfunctions of the Laplacian. *Adv Math* 18:102–107. [https://doi.org/10.1016/0001-8708\(75\)90003-1](https://doi.org/10.1016/0001-8708(75)90003-1)

- Horváth L, Kokoszka P (2012) *Inference for Functional Data with Applications*. Springer, New York
- Li D, Robinson PM, Shang HL (2019) Long-range dependent curve time series. *J Am Stat Assoc* 115:957–971
- Ma C, Malyarenko A (2020) Time varying isotropic vector random fields on compact two point homogeneous spaces. *J Theor Probab*. 33:319–339
- Marinucci D, Peccati G (2011) *Random fields on the Sphere. Representation, Limit Theorems and Cosmological Applications*. London Mathematical Society Lecture Note Series 389. Cambridge University Press, Cambridge
- Marinucci D, Rossi M, Vidotto A (2020) Non-universal fluctuations of the empirical measure for isotropic stationary fields on $\mathbb{S}^2 \times \mathbb{R}$. *Ann Appl Probab*. 31: 2311–2349
- Panaretos VM, Tavakoli S (2013) Fourier analysis of stationary time series in function space. *Ann Statist* 41:568–603
- Panaretos VM, Tavakoli S (2013) Cramér-Karhunen-Loève representation and harmonic principal component analysis of functional time series. *Stochastic Process their Appl* 123:2779–2807
- Pham T, Panaretos V (2018) Methodology and convergence rates for functional time series regression. *Statistica Sinica*. 28:2521–2539
- Rackauskas A, Suquet Ch (2011) Operator fractional brownian motion as limit of polygonal lines processes in Hilbert space. *Stochast Dyn* 11:49–70
- Ramm AG (2005) *Random Fields Estimation*. Longman Scientific & Technical, Harlow
- Rubín T, Panaretos VM (2020) Functional lagged regression with sparse noisy observations. *Journal of Time Series Analysis*. 41:858–882
- Rubín T, Panaretos VM (2020b) Spectral simulation of functional time series. *arXiv preprint [arXiv:2007.08458](https://arxiv.org/abs/2007.08458)*
- Ruiz-Medina MD (2022) Spectral analysis of long range dependence functional time series. *Fract Calculus Appl Anal* 25:1426–1458
- Tavakoli S (2014) *Fourier Analysis of Functional Time Series with Applications to DNA Dynamics*. Ph.D. dissertation, EPFL. Available at <https://doi.org/10.5075/epfl-thesis-6320>
- Tavakoli S, Panaretos VM (2016) Detecting and localizing differences in functional time series dynamics: a case study in molecular biophysics. *J Am Stat Assoc* 111:1020–1035

Publisher's Note Springer Nature remains neutral with regard to jurisdictional claims in published maps and institutional affiliations.